Satellite observations of the Alfvénic Transition from Weak to Strong Magnetohydrodynamic Turbulence

Siqi Zhao[12], Huirong Yan[12*], Terry Z. Liu[3*], Ka Ho Yuen[4], Huizi Wang[5]

[1]Deutsches Elektronen Synchrotron DESY, Platanenallee 6, D-15738, Zeuthen, Germany
[2]Institut für Physik und Astronomie, Universität Potsdam, D-14476, Potsdam, Germany
[3]Department of Earth, Planetary, and Space Sciences, University of California, Los Angeles, CA 90024, USA
[4]Theoretical Division, Los Alamos National Laboratory, Los Alamos, NM 87545, USA
[5]Centre for Shandong Key Laboratory of Optical Astronomy and Solar-Terrestrial Environment, Institute of Space Sciences, 264209, Shandong University, Weihai, People's Republic of China
[*]Corresponding author: huirong.yan@desy.de; terryliuzixu@ucla.edu

(submitted)

Plasma turbulence is a ubiquitous dynamical process that transfers energy across many spatial and temporal scales in astrophysical and space plasma systems[1–8]. Although the theory of anisotropic magnetohydrodynamic (MHD) turbulence has successfully described phenomena in nature, its core prediction of an Alfvénic transition from weak to strong MHD turbulence when energy cascades from large to small scales has not been observationally confirmed[9,10]. Here we report the first observational evidence for the Alfvénic weak-to-strong transition in MHD turbulence in the terrestrial magnetosheath using the four *Cluster* spacecraft. The observed transition indicates the universal existence of strong turbulence regardless of the initial level of MHD fluctuations. Moreover, the observations demonstrate that the nonlinear interactions of MHD turbulence play a crucial role in the energy cascade, widening the directions of the energy cascade and broadening the fluctuating frequencies. Our work takes a critical step toward understanding the complete picture of turbulence cascade, connecting the weak and strong MHD turbulence systems. It will have broad implications in star formation, energetic particle transport, turbulent dynamo, and solar corona or solar wind heating.

The theory of anisotropic MHD turbulence has been widely accepted and adopted in plasma systems, ranging from clusters of galaxies[3,4], the interstellar medium[5,6], accretion disks[7], the heliosphere[11,12], to nuclear fusion devices[8,13]. One of the most critical predictions of the theory is an Alfvénic transition from weak to strong turbulence when energy cascades from large to small scales[9,10]. The self-organized process from weak to strong turbulence is the cornerstone of understanding the energy cascade in the complete picture of MHD turbulence. In incompressible MHD (IMHD), when $\tau_A \ll \tau_{nl}$ (referred to as weak turbulence), the weak, three-wave interaction transfers energy to higher $k_\perp$, whereas no energy cascades to higher $k_\parallel$, where $\tau_A =$

$1/(k_\parallel V_A)$ is the linear Alfvén wave time, $\tau_{nl} = 1/(k_\perp \delta V_\perp)$ is the nonlinear cascade time, V_A is the Alfvén speed, $\delta V_\perp$ is the velocity fluctuation perpendicular to the mean magnetic field ($\mathbf{B}_0$), and $k_\perp$ and $k_\parallel$ are wavenumbers perpendicular and parallel to $\mathbf{B}_0$[9,14]. As turbulence cascades to smaller scales, the nonlinearity strengthens until reaching the critical balance ($\tau_A \sim \tau_{nl}$) at the transition scale (λ_{CB}). At scales smaller than λ_{CB}, Alfvén wave packets are statistically destroyed in one τ_A, and the non-resonant three-wave interaction is permitted, creating strong turbulence[9,15–17]. In compressible MHD (CMHD), small amplitude fluctuations can be decomposed into three eigenmodes (Alfvén, fast, and slow modes) in homogeneous plasma[18–22], wherein Alfvén modes show similar properties to those in the IMHD context, e.g., the Kolmogorov spectrum and scale-dependent Goldreich-Sridhar anisotropy[23,24]. Moreover, the cascade of Alfvén modes is almost independent of fast and slow modes[23].

Recent numerical simulations have confirmed the Alfvénic weak-to-strong transition in both IMHD turbulence and Alfvén modes decomposed from CMHD turbulence[19,25,26]. However, such a transition has not been observationally confirmed. Most astrophysical and space plasma is compressible, and density fluctuations cannot be neglected due to finite plasma β, i.e., the ratio between the plasma thermal pressure and magnetic pressure. Therefore, the terrestrial magnetosheath, filled with decelerated and compressed solar wind, provides an excellent and universal laboratory to study plasma turbulence[27,28]. In this study, we present the first observational evidence for the Alfvénic weak-to-strong transition in the terrestrial magnetosheath and estimate the transition scale λ_{CB} using four *Cluster* spacecraft data[29].

Here we analyze an event on 2-3 December 2003, during which time the *Cluster* spacecraft were located on the flank of magnetosheath around [1.2, 18.2, -5.7] R_E (Earth radius) in geocentric-solar-ecliptic (GSE) coordinates. The four spacecraft were flying in a tetrahedral formation with relative satellite separation $d_{sc} \sim 200$ km (~three times the proton gyro-radius). Fig. 1 shows an overview of the event observed by *Cluster*-1. Fig. 1a-b show the magnetic field (**B**) measured by the Fluxgate Magnetometer (FGM)[30] and the proton bulk velocity ($\mathbf{V}_p$) measured by the Cluster Ion Spectrometry (CIS)[31]. In Fig. 1c, the proton density (N_p) measured by CIS is consistent with the electron density measured by the Waves of High frequency and Sounder for Probing of Electron density by Relaxation (WHISPER)[32], cross-verifying the reliability of plasma data.

We set a moving time window with a length of five hours and a step size of five minutes. Fig. 1d shows the time series of spectral slopes of the trace magnetic and velocity power in the spacecraft-frame frequency $f_{sc} \sim [0.001\text{Hz}, 0.1 f_{ci}]$, where the proton gyro-frequency $f_{ci} \sim 0.24$ Hz (see Methods). We only analyze fluctuations with spectral slopes close to -5/3 or -3/2 because we focus on investigating the transition of energy cascade in fully developed plasma turbulence. The remaining magnetosheath fluctuations with spectra close to f_{sc}^{-1} are typically populated by uncorrelated

fluctuations[33,34] and are beyond the scope of the present paper. We choose the shorter interval between the two vertical dashed lines to eliminate the edge effects in wavelet transforms[35]. During this interval, the proton gyro-radius is r_{ci}~60 km, the proton inertial length is d_i~74 km, and the proton plasma is β_p~1.4. In Fig. 1f, the turbulent Alfvén number is $M_{A,turb}$~0.34, satisfying the assumption of small fluctuations. Besides, half of the relative amplitudes of magnetic field fluctuations are close to $M_{A,turb}$, suggesting substantial Alfvénic component. The average magnetic compressibility is $C_{\parallel}(f_{sc}) = \frac{|\delta B_{\parallel}(f_{sc})|^2}{|\delta B_{\parallel}(f_{sc})|^2+|\delta B_{\perp}(f_{sc})|^2}$~0.33, indicating the fluctuations are a mixture of Alfvén and compressible magnetosonic (fast and slow) modes[36], where $\delta B_{\parallel}$ and $\delta B_{\perp}$ are the fluctuating magnetic field parallel and perpendicular to $\mathbf{B}_0$.

We first extract Alfvénic fluctuations from turbulence based on their incompressibility and fluctuating directions perpendicular to $\mathbf{B}_0$. Then, we develop a new method on the basis of former studies[37,38] to obtain three-dimensional (3D) distributions of Alfvénic power at the MHD scales, allowing direct comparisons between observations and theory (see Methods). The structure of turbulence is described using 3D power distributions , i.e. magnetic power $P_{B_A}(k_{\perp}, k_{\parallel}, f_{sc})$ and velocity power $P_{V_A}(k_{\perp}, k_{\parallel}, f_{sc})$ (see Supplemental Material). The wavevectors are determined by combining the singular value decomposition method[37] (to obtain $\widehat{\boldsymbol{k}}_{SVD}$) and the multispacecraft timing method[38] (to obtain $\boldsymbol{k}_A$), allowing us to distinguish spatial and temporal evolutions without any spatiotemporal hypothesis, e.g., Taylor's hypothesis[39]. The combination of the two methods is valid only when $\boldsymbol{k}_A$ is roughly aligned with $\widehat{\boldsymbol{k}}_{SVD}$. Therefore, we present power distributions satisfying small angle θ between $\boldsymbol{k}_A$ and $\widehat{\boldsymbol{k}}_{SVD}$, i.e., θ=10°, 15°, 20°, 25°, and 30°. The spectral results are displayed by taking the data set with θ=30° as an example, in view of the slight effects of θ (see Supplemental Material).

Evidence for the Alfvénic weak-to-strong transition revealed from the *Cluster* observations

Change in wavenumber distributions of magnetic energy from purely perpendicular/2D cascade to Goldreich-Sridhar cascade.

The two-dimensional (2D) wavenumber distributions of magnetic energy are calculated by

$$P_{B_A}(k_{\perp}, k_{\parallel}) = \int_0^{\infty} P_{B_A}(k_{\perp}, k_{\parallel}, f_{sc}) df_{sc} . \quad (1)$$

$\hat{P}_{B_A}(k_{\perp}, k_{\parallel}) = P_{B_A}(k_{\perp}, k_{\parallel})/P_{B_A,max}$ is normalized by the maximum magnetic energy in all $(k_{\perp}, k_{\parallel})$ bins, displayed by the spectral image in Fig. 2a and by contours in Fig. 2b. Compared to the isotropic dotted curves, $\hat{P}_{B_A}(k_{\perp}, k_{\parallel})$ is prominently distributed

along the $k_\perp$ direction, suggesting a faster perpendicular cascade. This anisotropic behavior is more significant at higher wavenumbers, consistent with previous simulations[40] and observations[24,41].

Moreover, $\hat{P}_{B_A}(k_\perp, k_\parallel)$ is compared with 2D theoretical energy spectra in strong turbulence[6,9]

$$I_A(k_\perp, k_\parallel) \propto k_\perp^{-7/3} \exp\left(-\frac{L_0^{1/3}|k_\parallel|}{M_{A,turb}^{\frac{4}{3}} k_\perp^{\frac{2}{3}}}\right). \quad (2)$$

The injection scale L_0 is approximately estimated by the correlation time (T_c~1400 s) and rms fluctuating proton velocity perpendicular to $\mathbf{B}_0$ ($\delta V_{p\perp}$~ 33 km s^{-1}). $\hat{I}_A(k_\perp, k_\parallel) = I_A(k_\perp, k_\parallel)/I_{A,max}$ is normalized by the maximum magnetic energy in all $(k_\perp, k_\parallel)$ bins, displayed by color contours with black dashed curves in Fig. 2. The 2D distribution $\hat{P}_{B_A}(k_\perp, k_\parallel)$ shows two different properties: (1) At $k_\perp < 2 \times 10^{-4}\ km^{-1}$, $\hat{P}_{B_A}(k_\perp, k_\parallel)$ is almost unchanged with the increase of $k_\perp$ and is mainly concentrated at $k_\parallel < 7 \times 10^{-5}\ km^{-1}$, consistent with energy distributions in theoretical weak turbulence. (2) At $k_\perp > 2 \times 10^{-4}\ km^{-1}$, $\hat{P}_{B_A}(k_\perp, k_\parallel)$ starts to distribute to higher $k_\parallel$, and both the wavenumber distribution and intensity change of $\hat{P}_{B_A}(k_\perp, k_\parallel)$ are primarily consistent with $\hat{I}_A(k_\perp, k_\parallel)$. Besides, $\hat{P}_{B_A}(k_\perp, k_\parallel)$ is in good agreement with the Goldreich-Sridhar[9] scaling $k_\parallel \propto k_\perp^{2/3}$ (marked by pink dotted lines). Thus, the properties at $k_\perp > 2 \times 10^{-4}\ km^{-1}$ are closer to those in strong turbulence. The change from purely stretching along the $k_\perp$ direction (2D) to following the Goldreich-Sridhar[9] scaling $k_\parallel \propto k_\perp^{2/3}$ in wavenumber space reveals a possible transition in the energy cascade.

Sharp change in spectral slopes of magnetic energy spectral density from wave-like (-2) to Kolmogorov-like (-5/3).

Fig. 3a shows the compensated spectra $k_\perp^{5/3} E_{B_A}(k_\perp)$, where the magnetic energy spectral density is defined as $E_{B_A}(k_\perp) = \frac{1}{2}\frac{\delta B_A^2(k_\perp)}{k_\perp}$, and $\delta B_A^2(k_\perp)$ is magnetic energy density at $k_\perp$ (see Methods). In Zone (2), $k_\perp^{5/3} E_{B_A}(k_\perp)$ is roughly consistent with

$k_\perp^{5/3-2}$ (marked by the black dashed line), indicating that the spectral slopes of $E_{B_A}(k_\perp)$ are around -2. Whereas in Zone (3), $k_\perp^{5/3}E_{B_A}(k_\perp)$ is almost flat at some $k_\perp$, suggesting that $E_{B_A}(k_\perp)$ satisfies the Kolmogorov scaling ($E_{B_A}(k_\perp) \propto k_\perp^{-5/3}$). The sharp change in spectral slopes of $E_{B_A}(k_\perp)$ from -2 to -5/3 is apparent evidence for the transition of turbulence regimes[9,25,26].

Nonlinear parameter shows a Goldreich-Sridhar[9] scaling in terms of wavenumber.

Fig. 3b shows the variation between $k_\parallel$ versus $k_\perp$ estimated by taking the same values of Alfvénic magnetic energy. As $k_\perp$ increases, $k_\parallel$ is approximately stable at $k_\parallel \sim 7 \times 10^{-5}\, km^{-1}$ (marked by the horizontal line) in Zone (1). In contrast, the variation of $k_\perp$ versus $k_\parallel$ agrees with the Goldreich-Sridhar scaling $k_\parallel \propto k_\perp^{2/3}$ (marked by the purple line) in Zone (3). Fig. 3c shows $k_\perp - k_\parallel$ distributions of nonlinearity parameter $\chi_{B_A}(k_\perp, k_\parallel) \sim \frac{k_\perp \delta B_A(k_\perp, k_\parallel)}{k_\parallel B_0}$, which is one of the most critical parameters in distinguishing weak from strong turbulence[8,10] (see Methods). At parallel and perpendicular wavenumbers with the same magnetic energy (Fig. 3b), χ_{B_A} is much less than unity in Zone (1), whereas χ_{B_A} increases approaching unity and follows the scaling $k_\parallel \propto k_\perp^{2/3}$ in Zone (3). These results suggest a transition from weak to strong nonlinear interactions, in good agreement with current theory and simulations[9,25,26].

With the measurements of velocity fluctuations, we observe a similar transition process (see Supplemental Material). The transition scale (λ_{CB}) is estimated by the smallest perpendicular wavenumber of strong turbulence ($k_{\perp,CB}$), where $\lambda_{CB} \sim 1/k_{\perp,CB}$. For both magnetic field and velocity data, $k_{\perp,CB}$ is around $3 \times 10^{-4}\, km^{-1}$, marked by the second vertical lines in Fig. 3 and Figure S4. The consistency in the transition scales estimated by magnetic field and velocity measurements further confirms the reliability of our findings.

Here, we do not discuss fluctuations in Zone (2) and (4) of Fig. 3b-c for several reasons. A significant perturbation is present in Zone (2), resulting from the local magnetic energy enhancements around $k_\perp \sim 1.8 \times 10^{-4}\, km^{-1}$ (Fig. 2), making the simultaneous existence of strong nonlinearity ($\chi_{B_A} \sim 1$ at $[k_\perp, k_\parallel] \sim [1.8 \times 10^{-4}, 4 \times 10^{-5}] km^{-1}$ and weak nonlinearity ($\chi_{B_A} \ll 1$ at $[k_\perp, k_\parallel] \sim [2.3 \times 10^{-4}, 1 \times 10^{-4}] km^{-1}$. Thus, we deduce that the weak-to-strong transition is more likely to occur in a 'region' rather than a critical wavenumber. The magnetic energy in Zone (4) is almost three orders of magnitude smaller than that in Zone (1) (Fig. 2), and thus the quantitative analysis is questionable. Moreover, the deviations of $\theta - 10^\circ$ and $\theta -$

15° data sets in Zone (3) of Fig. 3b are likely due to the limited data samples (see Supplemental Material). The uncertainties mentioned above do not affect our main conclusions.

The change from single-frequency (~Alfvén frequency) to broadening-frequency fluctuations

Fig. 4 presents the $k_{\perp} - f_{rest}$ distribution of magnetic energy, where f_{rest} is the observed frequency in the plasma flow frame. At $k_{\perp} < 5 \times 10^{-5}\, km^{-1}$, f_{rest} approaches to be concentrated around the theoretical frequencies of Alfvén modes[42] f_A, where $f_A = \frac{|k_{\parallel} V_A|}{2\pi}$ are marked by the horizontal dotted lines with error bars. At $k_{\perp} > 1 \times 10^{-4}\, km^{-1}$, the range of f_{rest} broadens, and a majority of fluctuating frequencies deviate from f_A. Nevertheless, the boundary frequencies of these fluctuations are roughly consistent with the scaling $f_{rest} \propto k_{\perp}^{2/3}$ (marked by the pink dashed line), indicating that magnetic energy at these wavenumbers satisfies the scaling $k_{\parallel} \propto k_{\perp}^{2/3}$ due to $f_{rest} \propto k_{\parallel}$ for Alfvén modes. These results suggest that Alfvénic fluctuations with strong nonlinear interactions do not agree with linear dispersion relations, but they still satisfy the wavenumber scaling of Alfvén modes. The change from the single-frequency to broadening-frequency fluctuations with the increasing $k_{\perp}$ suggests a possible transition of turbulence regimes.

Implications of direct confirmation of Alfvénic weak-to-strong transition to astrophysical and space turbulence research

In summary, the evidence presented above directly confirms the theoretical prediction of the Alfvénic weak-to-strong transition when MHD turbulence cascades from large to small scales, e.g., the changes of power spectral slopes (Fig. 3a) and the nonlinear parameter (Fig. 3c). The transition scales estimated by all evidence (listed in Table 1) are approximately consistent. Our observations demonstrate that the Alfvénic transition to strong turbulence with the critical balance is bound to occur with the increase of nonlinearity, regardless of the initial level of MHD fluctuations, pinpointing the universality of strong turbulence. Moreover, our observations show that turbulence can self-organize from 2D wave-like fluctuations to 3D strong turbulence. Thus, the debate on 2D turbulence[43,44] vs. turbulence with scale-dependent anisotropy[9,40] can be settled with the discovery of the Alfvénic transition. We want to point out that the plasma parameters in the analyzed event are common, and the Alfvénic weak-to-strong transition can occur in other astrophysical and space plasma systems. The impact of our findings goes beyond the study of turbulence itself to particle transport and acceleration, magnetic reconnection, star formation, and all the other relevant fields.

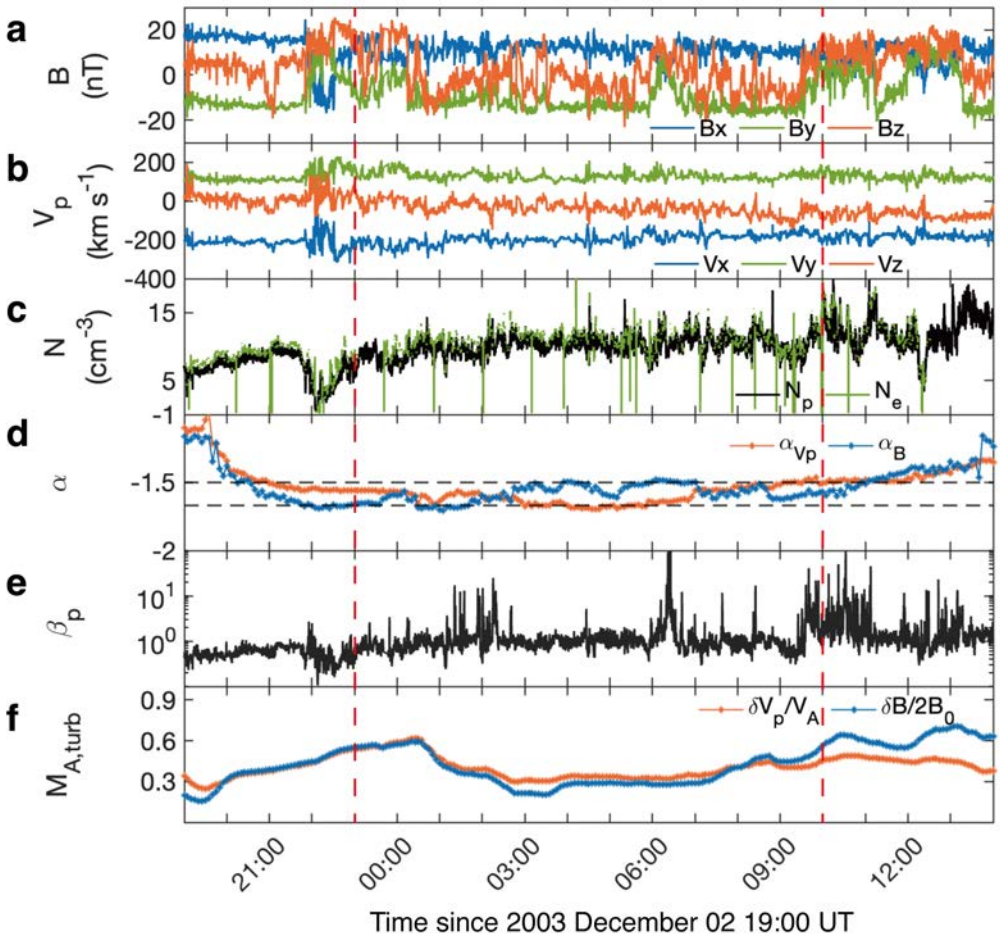

Fig. 1 | An overview of fluctuations measured by *Cluster*-1 in the terrestrial magnetosheath on 2-3 December 2003. The data are displayed in GSE coordinates. **a**, magnetic field components (B_x, B_y and B_z); **b**, proton bulk velocity (V_x, V_y and V_z); **c**, proton and electron density; **d**, spectral slopes (α) of magnetic field and velocity fluctuations between 0.001 Hz and 0.1f_{ci}. The two horizontal lines represent $\alpha = -\frac{5}{3}$ and $\alpha = -\frac{3}{2}$. **e**, The proton plasma β_p. **f**, The turbulent Alfvén Mach number ($M_{A,turb} = \frac{\delta V_p}{V_A}$) and half of the relative amplitudes of the magnetic field ($\frac{\delta B}{2B_0}$), where δV_p and δB are rms proton velocity and magnetic field fluctuations, respectively. The fluctuations analyzed in detail are during 23:00-10:00 on 2-3 December, marked between the two vertical dashed lines.

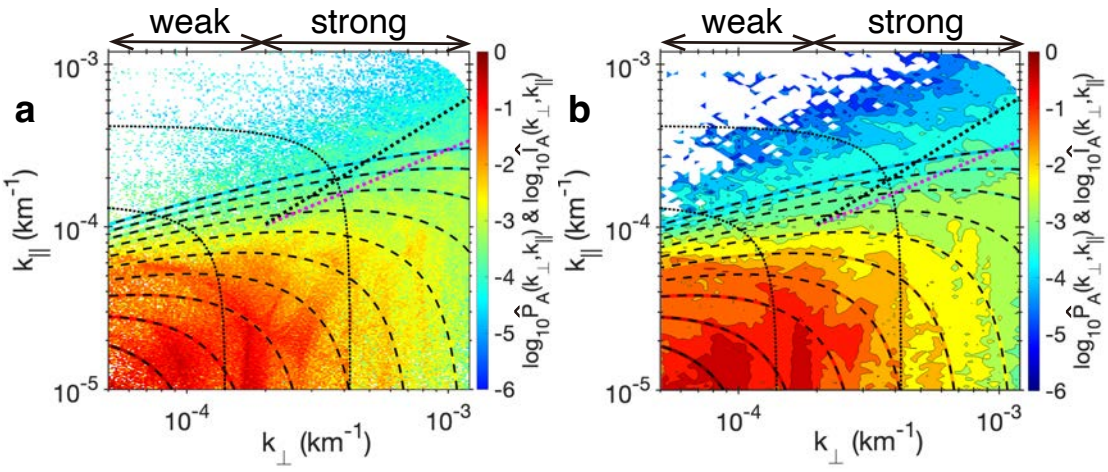

Fig. 2 | The comparison between wavenumber distributions of Alfvénic magnetic energy $\hat{P}_{B_A}(k_\perp, k_\parallel)$ and theoretical energy spectra[9] $\hat{I}_A(k_\perp, k_\parallel)$. **a**, The 2D spectral image represents $\hat{P}_{B_A}(k_\perp, k_\parallel)$. The color contours with black dashed curves represent $\hat{I}_A(k_\perp, k_\parallel)$. **b**, For the contour continuity, we present the contours of $\hat{P}_{B_A}(k_\perp, k_\parallel)$ with a low resolution. The filled 2D contours represent $\hat{P}_{B_A}(k_\perp, k_\parallel)$. $\hat{I}_A(k_\perp, k_\parallel)$ is displayed by color contours with black dashed curves. **a**,**b**, $\hat{I}_A(k_\perp, k_\parallel)$ is in the same color map as $\hat{P}_{B_A}(k_\perp, k_\parallel)$. The black dotted curves mark $k = \sqrt{k_\parallel^2 + k_\perp^2} = 0.01/d_i$ and $0.03/d_i$. The pink and black dotted lines represent the scaling $k_\parallel \propto k_\perp^{2/3}$ and $k_\parallel \propto k_\perp$, respectively. These figures utilize the data set with θ=30°.

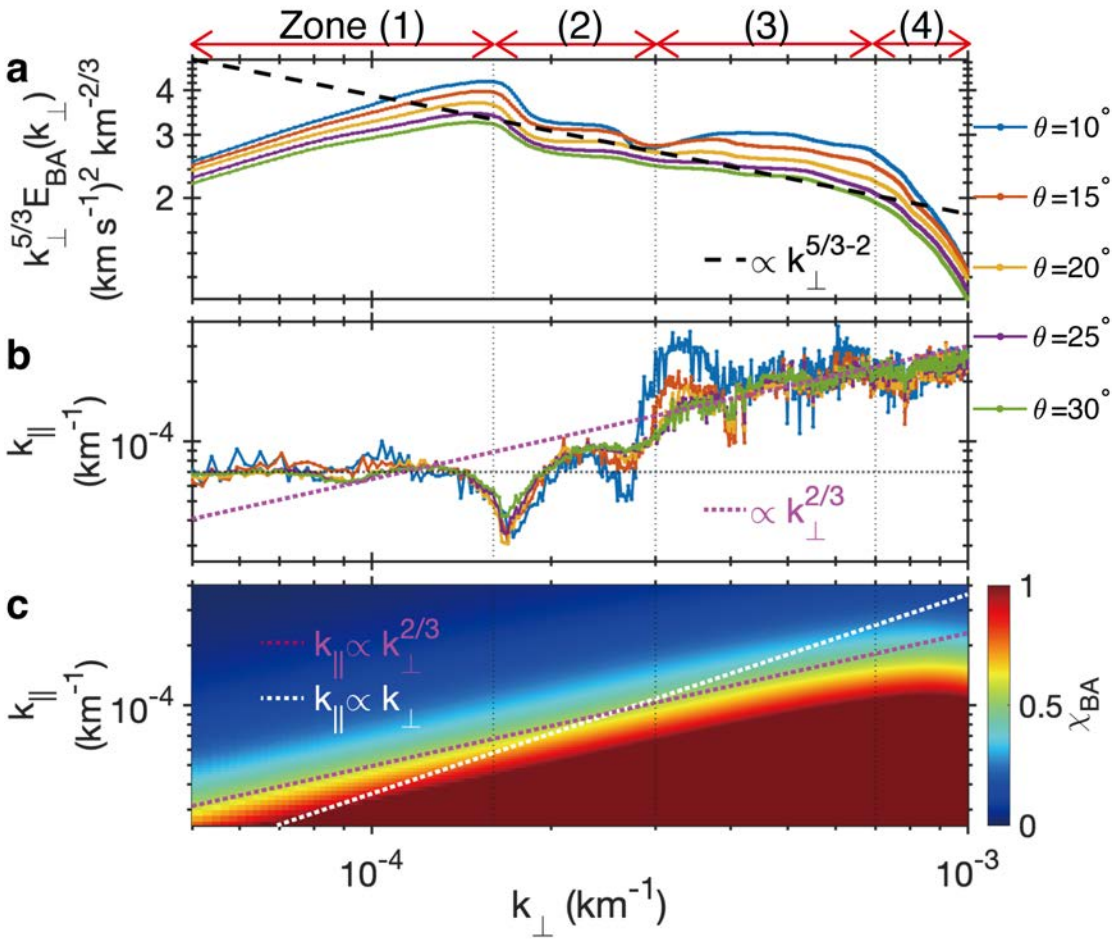

Fig. 3 | **a**, The compensated spectra $k_\perp^{5/3}E_{B_A}(k_\perp)$. The magnetic field fluctuations are in Alfvén speed units to facilitate comparison to velocity fluctuations. The black dashed line represents $k_\perp^{5/3}E_{B_A}(k_\perp) \propto k_\perp^{5/3-2}$ used as the reference. **b**, The variation of $k_\parallel$ versus $k_\perp$. The purple dotted line represents the scaling $k_\parallel \propto k_\perp^{2/3}$. The horizontal dotted line represents $k_\parallel = 7\times10^{-5}\ km^{-1}$. **a**-**b**, Blue, red, yellow, purple, and green colors represent observations from data sets with θ=10°, 15°, 20°, 25°, and 30°, respectively. **c**, The nonlinearity parameter $\chi_{B_A}(k_\perp, k_\parallel)$. The purple and white dotted lines represent the scaling $k_\parallel \propto k_\perp^{2/3}$ and $k_\parallel \propto k_\perp$, respectively. χ_{B_A} spectrum is calculated using the data set with θ=30°. The $k_\perp$ distributions are roughly divided into four Zones: Zone (1) $5\times10^{-5} < k_\perp < 1.6\times10^{-4}\ km^{-1}$, Zone (2) $1.6\times10^{-4} < k_\perp < 3\times10^{-4}\ km^{-1}$, Zone (3) $3\times10^{-4} < k_\perp < 7\times10^{-4}\ km^{-1}$, and Zone (4) $7\times10^{-4} < k_\perp < 1\times10^{-3}\ km^{-1}$. The first, second, and third vertical dotted lines are around the maximum of $k_\perp^{5/3}E_{B_A}(k_\perp)$, the beginning of flattened $k_\perp^{\frac{5}{3}}E_{B_A}(k_\perp)$, and the

end of flattened $k_\perp^{5/3} E_{B_A}(k_\perp)$, respectively.

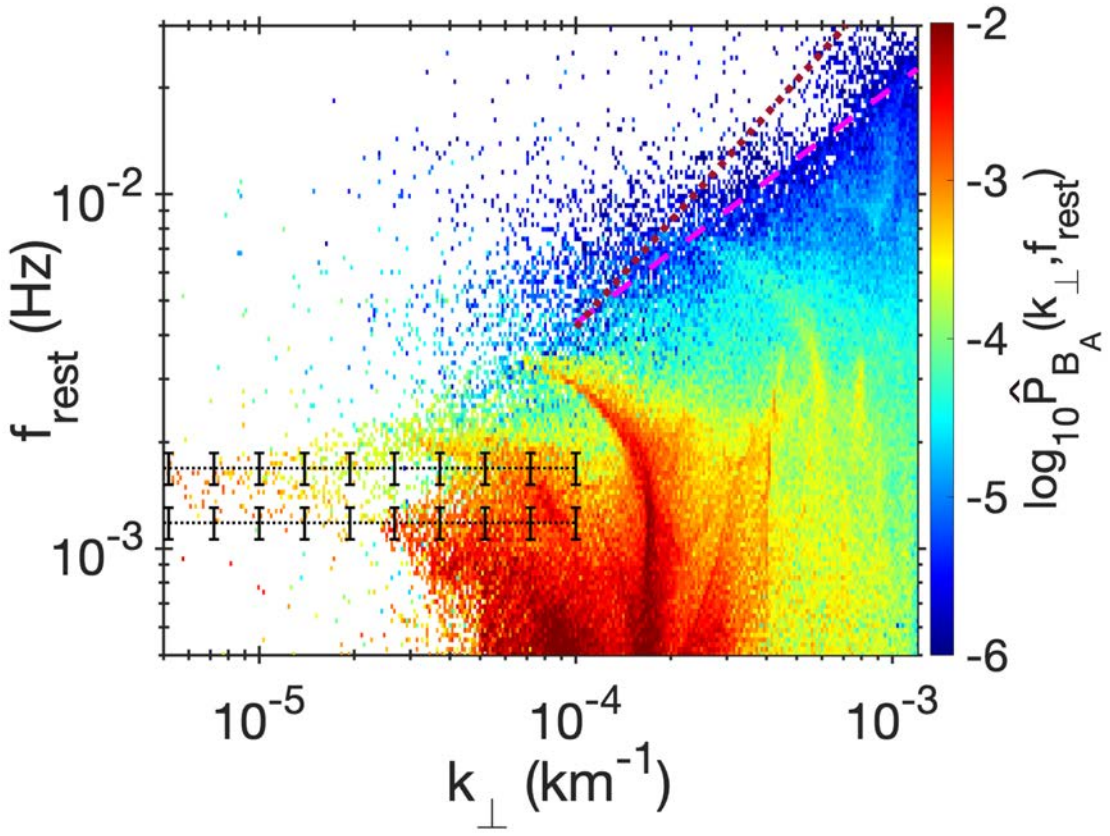

Fig. 4 | The $k_\perp - f_{rest}$ distribution of Alfvénic magnetic energy in the plasma flow frame. $\hat{P}_{B_A}(k_\perp, f_{rest}) = P_{B_A}(k_\perp, f_{rest})/P_{B_A,max}$ is normalized by the maximum magnetic energy in all $(k_\perp, f_{rest})$ bins. The pink and red dotted lines represent the scaling $f_{rest} \propto k_\perp^{2/3}$ and $f_{rest} \propto k_\perp$. The two horizontal dotted lines with error bars represent the theoretical Alfvénic frequencies $f_A = \frac{|k_\parallel V_A|}{2\pi}$. $k_\parallel$ are estimated by $k_\parallel$ values in Zone (1) of Fig. 3b and Figure S4b, where $k_\parallel \sim 7 \times 10^{-5}\ km^{-1}$ and $1 \times 10^{-4}\ km^{-1}$. f_A uncertainties are estimated by the standard value of the Alfvén speed V_A, where $V_A = 106 \pm 11\ km\ s^{-1}$. This figure utilizes the data set with θ=30°.

	Weak turbulence	Strong turbulence
The wavenumber distributions of magnetic field fluctuations	Purely perpendicular cascade $k_\perp < 2 \times 10^{-4}\ km^{-1}$	Goldreich-Sridhar cascade $k_\perp > 2 \times 10^{-4}\ km^{-1}$
Spectral slopes of magnetic energy	Wave-like (-2) $1.6 \times 10^{-4} < k_\perp < 3 \times 10^{-4}\ km^{-1}$	Kolmogorov-like (-5/3) $3 \times 10^{-4} < k_\perp < 7 \times 10^{-4}\ km^{-1}$
Nonlinearity parameter (χ_B)	$\chi_B \ll 1$ $k_\perp < 1 \times 10^{-4}\ km^{-1}$	$\chi_B \sim 1$ & $\chi_B \geq 1$ $3 \times 10^{-4} < k_\perp < 7 \times 10^{-4}\ km^{-1}$
Frequency-wavenumber distributions	Single-frequency fluctuations approaching to f_A $k_\perp < 5 \times 10^{-5}\ km^{-1}$	Broadening-frequency fluctuations with $f_{rest} \propto {k_\perp}^{2/3}$ boundary $k_\perp > 1 \times 10^{-4}\ km^{-1}$

Table 1. **The transition wavenumbers are estimated by all evidence.**

Methods

Geocentric-solar-ecliptic (GSE) coordinates

We use the GSE coordinate in this study. X_{GSE} points towards the Sun from the Earth, Z_{GSE} orients along the ecliptic north pole, and Y_{GSE} completes a right-handed system.

The trace power spectral densities

The trace magnetic and velocity power spectral densities ($P_B = P_{B,X} + P_{B,Y} + P_{B,Z}$ and $P_V = P_{V,X} + P_{V,Y} + P_{V,Z}$) are calculated by applying the fast Fourier transform with three-point centered smoothing in GSE coordinates. We choose the intermediate instant of each time window as the time point where the spectral slope varies with time.

Alfvén mode decomposition

We calculate 3D wavenumber distributions of magnetic and velocity power following our previous work[24]. The mode decomposition method is consistent with numerical simulation of CMHD turbulence, conducive to direct comparison with their results[19].

First, we obtain wavelet coefficients of magnetic field and velocity fluctuations by Morlet-wavelet transforms in GSE coordinates[35]. To eliminate the edge effect due to

finite-length time series, we perform wavelet transforms twice the length of the studied period and cut off the affected periods.

Second, based on the linearized Gauss's law for magnetism ($\boldsymbol{k}_{SVD} \cdot \delta\boldsymbol{B} = 0$), the singular value decomposition (SVD) method of magnetic wavelet coefficients is used to calculate the wavevector direction[37] ($\boldsymbol{k}_{SVD}(t, f_{sc})$), where $\delta\boldsymbol{B}$ represents magnetic field fluctuations. Since relative satellite separations are much shorter than the half-wavelength at the MHD scales, the properties of fluctuations simultaneously measured by the four *Cluster* spacecraft are similar. Thus, we average the wavevector and background magnetic field over four spacecraft: $\boldsymbol{k}_{SVD} = \frac{1}{4}(\widehat{\boldsymbol{k}}_{SVD,C1} + \widehat{\boldsymbol{k}}_{SVD,C2} + \widehat{\boldsymbol{k}}_{SVD,C3} + \widehat{\boldsymbol{k}}_{SVD,C4})$ and $\boldsymbol{B}_0 = \frac{1}{4}\left(\boldsymbol{B}_{0,C1} + \boldsymbol{B}_{0,C2} + \boldsymbol{B}_{0,C3} + \boldsymbol{B}_{0,C4}\right)$, where C1, C2, C3, and C4 denote the four *Cluster* spacecraft.

Third, we extract the Alfvénic components from velocity fluctuations ($\delta\boldsymbol{V}_p$) based on their incompressibility ($\widehat{\boldsymbol{k}}_{SVD} \cdot \delta\boldsymbol{V}_p = 0$) and perpendicular fluctuating directions ($\widehat{\boldsymbol{b}}_0 \cdot \delta\boldsymbol{V}_p = 0$) in wavenumber space, where $\widehat{\boldsymbol{k}}_{SVD} = \frac{\boldsymbol{k}_{SVD}}{|\boldsymbol{k}_{SVD}|}$ and $\widehat{\boldsymbol{b}}_0 = \frac{\boldsymbol{B}_0}{|\boldsymbol{B}_0|}$ are the unit vectors of $\boldsymbol{k}_{SVD}$ and $\boldsymbol{B}_0$, respectively. Moreover, we extract Alfvénic magnetic field fluctuations based on $\widehat{\boldsymbol{k}}_{SVD} \cdot \delta\boldsymbol{B} = 0$ and $\widehat{\boldsymbol{b}}_0 \cdot \delta\boldsymbol{B} = 0$, according to the linearized induction equation

$$\omega\delta\boldsymbol{B} = \boldsymbol{k} \times \left(\boldsymbol{B}_0 \times \delta\boldsymbol{V}_p\right) \sim |\boldsymbol{k}|\widehat{\boldsymbol{k}}_{SVD} \times \left(\boldsymbol{B}_0 \times \delta\boldsymbol{V}_p\right), \quad (1)$$

where $\boldsymbol{k}$ is the wavevector. Thus, Alfvénic velocity and magnetic field fluctuations are in the same direction ($\frac{\widehat{\boldsymbol{k}}_{SVD} \times \widehat{\boldsymbol{b}}_0}{|\widehat{\boldsymbol{k}}_{SVD} \times \widehat{\boldsymbol{b}}_0|}$) (see Schematic in Supplemental Material).

Fourth, the Alfvénic magnetic power averaged over four spacecraft at each time t and f_{sc} is given by

$$P_{B_A}(t, f_{sc}) = \frac{1}{4}\left(W_{B_A,C1}{W_{B_A,C1}}^* + W_{B_A,C2}{W_{B_A,C2}}^* + W_{B_A,C3}{W_{B_A,C3}}^* + W_{B_A,C4}{W_{B_A,C4}}^*\right) (2).$$

The Alfvénic velocity power measured by C1 at each time t and f_{sc} is given by

$$P_{V_A}(t, f_{sc}) = W_{V_A,C1}{W_{V_A,C1}}^* \quad (3).$$

Fifth, since the SVD method only determines the wavevector direction and cannot determine wavenumbers, we further calculate wavevectors ($\boldsymbol{k}_A(t, f_{sc})$) using the multispacecraft timing analysis based on phase differences between the Alfvénic magnetic field from four spacecraft[38]. The phase differences are determined by six cross-correlations[35], i.e., $W_{B_A}^{12} = \langle W_{B_A,C1}{W_{B_A,C2}}^* \rangle$, $W_{B_A}^{13} = \langle W_{B_A,C1}{W_{B_A,C3}}^* \rangle$, $W_{B_A}^{14} =$

$\langle W_{B_A,C1} {W_{B_A,C4}}^* \rangle$, $W_{B_A}^{23} = \langle W_{B_A,C2} {W_{B_A,C3}}^* \rangle$, $W_{B_A}^{24} = \langle W_{B_A,C2} {W_{B_A,C4}}^* \rangle$, and $W_{B_A}^{34} = \langle W_{B_A,C3} {W_{B_A,C4}}^* \rangle$. The angular brackets denote a time average over 256 s, to obtain reliable phase differences. Besides, magnetic field data for timing analysis are interpolated to a time resolution of $1/2^3$ samples s^{-1}, to ensure sufficient time resolutions.

The combination of the SVD method and multispacecraft timing analysis allows us to determine wavevectors independent of any spatiotemporal hypothesis, e.g., Taylor's hypothesis[39]. However, this combination is valid only when $\boldsymbol{k}_A$ is aligned with $\widehat{\boldsymbol{k}}_{SVD}$. Under such a condition, the extraction process (Step 3) is reliable. The observations show that $\widehat{\boldsymbol{k}}_{SVD}$ are not entirely aligned with $\boldsymbol{k}_A$, indicating that not all fluctuations are aligned with the minimum singular value of the magnetic field and satisfy $f_{sc} \propto k$ hypothesis. In contrast, the fluctuations are more likely a mixture of multiple modes with different dispersion relations. Therefore, we only analyze fluctuations with small angle θ between $\widehat{\boldsymbol{k}}_{SVD}$ and $\boldsymbol{k}_A$, generating five data sets with θ=10°, 15°, 20°, 25°, and 30°.

Sixth, the frequency $f_{rest}(t, f_{sc})$ is obtained by correcting the Doppler shift $f_{rest} = f_{sc} - \frac{\boldsymbol{k}_A \cdot \boldsymbol{V}}{2\pi}$, where f_{rest} is the frequency in the plasma flow frame, $\boldsymbol{V}$ is roughly equivalent to the proton bulk velocity ($\boldsymbol{V}_p$) due to the slow spacecraft speed. This study utilizes the representation of absolute frequencies:

$$(f_{rest}, \boldsymbol{k}_A) = \begin{cases} (f_{rest}, \boldsymbol{k}_A), & \text{for } f_{rest} > 0 \\ (-f_{rest}, -\boldsymbol{k}_A), & \text{for } f_{rest} < 0 \end{cases}. \quad (4)$$

Considering the applicability of MHD theory and measurement limitations, we analyze fluctuations satisfying $\frac{1}{100 * d_{sc}} < k < min\left(\frac{0.1}{max\,(d_i, r_{ci})}, \frac{2\pi}{2d_{sc}}\right)$ and $\frac{2}{t^*} < f_{rest} < \frac{1}{2} f_{ci}$, where d_{sc} represents relative satellite separations, $min(*)$ represents the minimum value, $max(*)$ represents the maximum value, d_i is proton inertial length, r_{ci} is proton gyro-radius, and t^* is the duration studied. The Alfvénic power is set to zero beyond this wavenumber, frequency, and angle θ range and is averaged over all valid time points at each f_{sc}.

Finally, we construct a set of 400×400×400 bins to obtain wavenumber distributions of magnetic (velocity) power $P_{B_A}(k_\perp, k_\parallel, f_{sc})$ ($P_{V_A}(k_\perp, k_\parallel, f_{sc})$), where the parallel wavenumber is $k_\parallel = \boldsymbol{k}_A \cdot \widehat{\boldsymbol{b}}_0$, and the perpendicular wavenumber is $k_\perp = \sqrt{\boldsymbol{k}_A^2 - k_\parallel^2}$. Each bin subtends approximately the same $k_\perp$, $k_\parallel$, and f_{sc}. The maximum wavenumber is set as $k_{max} = 1.1 \times \frac{0.1}{d_i}$, and the step length of each bin is $dk = \frac{k_{max}}{400}$.

Alfvén speed units

For comparison, this study presents the fluctuating magnetic field in Alfvén speed units, which is normalized by $\sqrt{\mu_0 m_p N_0}$, where μ_0 is the vacuum permeability, m_p is the

proton mass, and N_0 is the mean proton density.

Magnetic energy spectral density

This study defines the energy spectral density of magnetic field as $E_{B_A}(k_\perp) = \frac{1}{2}\frac{\delta B_A^2(k_\perp)}{k_\perp}$, where the Alfvénic magnetic energy density is calculated by $\delta B_A^2(k_\perp) = 2 \times \sum_{k_\perp=k_\perp}^{k_\perp\to\infty} \sum_{k_\parallel=0}^{k_\parallel\to\infty} \int_0^\infty P_{B_A}(k_\perp, k_\parallel, f_{sc}) df_{sc}$.

The nonlinearity parameter

The nonlinearity parameter is approximately estimated by $\chi_{B_A}(k_\perp, k_\parallel) \sim \frac{k_\perp \delta B_A(k_\perp, k_\parallel)}{k_\parallel B_0}$, where the Alfvénic magnetic energy density is calculated by $\delta B_A^2(k_\perp, k_\parallel) = \sum_{k_\perp=k_\perp}^{k_\perp\to\infty} \sum_{k_\parallel=k_\parallel}^{k_\parallel\to\infty} \int_0^\infty P_{B_A}(k_\perp, k_\parallel, f_{sc})\, df_{sc}$, and B_0 in Alfvén speed units is around 106 km/s.

The frequency-wavenumber distribution of magnetic energy

The frequency-wavenumber distribution of magnetic energy is approximately estimated by $P_{B_A}(k_\perp, f_{sc}) \sim \sum_{k_\parallel=0}^{k_\parallel\to\infty} P_{B_A}(k_\perp, k_\parallel, f_{sc}) \Delta f_{sc}$ and transformed into the plasma flow frame by correcting the Doppler shift $f_{rest} = f_{sc} - \frac{\boldsymbol{k_A \cdot V}}{2\pi}$.

Data Availability

The *Cluster* data are available at https://cdaweb.gsfc.nasa.gov.

Reference

1. Bruno, R. & Carbone, V. The Solar Wind as a Turbulence Laboratory. *Living Rev Sol Phys* **10**, (2013).

2. Verscharen, D., Klein, K. G. & Maruca, B. A. The multi-scale nature of the solar wind. *Living Rev Sol Phys* **16**, 5 (2019).

3. Brunetti, G. & Lazarian, A. Compressible turbulence in galaxy clusters: Physics and stochastic particle re-acceleration. *Mon Not R Astron Soc* **378**, 245–275 (2007).

4. Brunetti, G. & Lazarian, A. Acceleration of primary and secondary particles in galaxy clusters by compressible MHD turbulence: From radio haloes to gamma-rays. *Mon Not R Astron Soc* **410**, 127–142 (2011).

5. Yan, H. & Lazarian, A. Scattering of Cosmic Rays by Magnetohydrodynamic Interstellar Turbulence. *Phys Rev Lett* **89**, 281102 (2002).

6. Yan, H. & Lazarian, A. Cosmic-Ray Propagation: Nonlinear Diffusion Parallel and Perpendicular to Mean Magnetic Field. *Astrophys J* **673**, 942–953 (2008).

7. Balbus, S. A. & Hawley, J. F. Instability, turbulence, and enhanced transport in accretion disks. *Rev Mod Phys* **70**, 1–53 (1998).

8. Diamond, P. H., Itoh, S.-I., Itoh, K. & Hahm, T. S. Zonal flows in plasma—a review. *Plasma Phys Control Fusion* **47**, R35–R161 (2005).

9. Goldreich, P. & Sridhar, S. Toward a theory of interstellar turbulence. 2: Strong alfvenic turbulence. *Astrophys J* **438**, 763 (1995).

10. Howes, G. G., Tenbarge, J. M. & Dorland, W. A weakened cascade model for turbulence in astrophysical plasmas. *Phys Plasmas* **18**, (2011).

11. Tu, C. Y. & Marsch, E. MHD structures, waves and turbulence in the solar wind: Observations and theories. *Space Sci Rev* **73**, 1–210 (1995).

12. Chen, C. H. K. *et al.* The Evolution and Role of Solar Wind Turbulence in the Inner Heliosphere. *Astrophys J Suppl Ser* **246**, 53 (2020).

13. Dimits, A. M. *et al.* Comparisons and physics basis of tokamak transport models and turbulence simulations. *Physics of Plasmas* vol. 7 969–983 Preprint at https://doi.org/10.1063/1.873896 (2000).

14. Shebalin, J. V. & Montgomery, D. Anisotropy in Mhd Turbulence Due to a Mean Magnetic Field. *J Plasma Phys* **29**, 525–547 (1983).

15. Gan, Z., Li, H., Fu, X. & Du, S. On the Existence of Fast Modes in Compressible

Magnetohydrodynamic Turbulence. *Astrophys J* **926**, 222 (2022).

16. Mallet, A., Schekochihin, A. A. & Chandran, B. D. G. Refined critical balance in strong alfvénic turbulence. *Mon Not R Astron Soc Lett* **449**, L77–L81 (2015).

17. Fu, X., Li, H., Gan, Z., Du, S. & Steinberg, J. Nature and Scalings of Density Fluctuations of Compressible Magnetohydrodynamic Turbulence with Applications to the Solar Wind. *Astrophys J* **936**, 127 (2022).

18. Cho, J. & Lazarian, A. Compressible magnetohydrodynamic turbulence: Mode coupling, scaling relations, anisotropy, viscosity-damped regime and astrophysical implications. *Mon Not R Astron Soc* **345**, 325–339 (2003).

19. Makwana, K. D. & Yan, H. Properties of Magnetohydrodynamic Modes in Compressively Driven Plasma Turbulence. *Phys Rev X* **10**, 31021 (2020).

20. Zhu, X., He, J., Verscharen, D., Duan, D. & Bale, S. D. Wave Composition, Propagation, and Polarization of Magnetohydrodynamic Turbulence within 0.3 au as Observed by Parker Solar Probe. *Astrophys J* **901**, L3 (2020).

21. Chaston, C. C. *et al.* MHD Mode Composition in the Inner Heliosphere from the Parker Solar Probe 's First Perihelion. *Astrophys J Suppl Ser* **246**, 71 (2020).

22. Zhao, S. Q., Yan, H., Liu, T. Z., Liu, M. & Shi, M. Analysis of Magnetohydrodynamic Perturbations in the Radial-field Solar Wind from Parker Solar Probe Observations. *Astrophys J* **923**, 253 (2021).

23. Cho, J. & Lazarian, A. Compressible magnetohydrodynamic turbulence: Mode coupling, scaling relations, anisotropy, viscosity-damped regime and astrophysical implications. *Mon Not R Astron Soc* **345**, 325–339 (2003).

24. Zhao, S. Q., Yan, H., Liu, T. Z., Liu, M. & Wang, H. Multispacecraft Analysis of the Properties of Magnetohydrodynamic Fluctuations in Sub-Alfvénic Solar Wind Turbulence at 1 au. *Astrophys J* **937**, 102 (2022).

25. Verdini, A. & Grappin, R. Transition from weak to strong cascade in MHD turbulence. *Phys Rev Lett* **109**, 1–5 (2012).

26. Meyrand, R., Galtier, S. & Kiyani, K. H. Direct Evidence of the Transition from Weak to Strong Magnetohydrodynamic Turbulence. *Phys Rev Lett* **116**, 1–5 (2016).

27. Schwartz, S. J., Burgess, D. & Moses, J. J. Low-frequency waves in the Earth's magnetosheath: Present status. *Ann Geophys* **14**, 1134–1150 (1997).

28. Zhao, S. Q. *et al.* Observation of a Large-Amplitude Slow Magnetosonic Wave in the Magnetosheath. *J Geophys Res Space Phys* **124**, 10200–10208 (2019).

29. Escoubet, C. P., Fehringer, M. & Goldstein, M. The Cluster mission. *Ann Geophys* **19**, (2001).

30. Balogh, A. *et al.* The cluster magnetic field investigation. *Space Sci Rev* **79**, 65–91 (1997).

31. Rème, H. *et al.* First multispacecraft ion measurements in and near the Earth's magnetosphere with the identical Cluster ion spectrometry (CIS) experiment. *Ann Geophys* **19**, 1303–1354 (2001).

32. Décréau, P. M. E. *et al.* Whisper, a resonance sounder and wave analyser: Performances and perspectives for the Cluster mission. *Space Sci Rev* **79**, 157–193 (1997).

33. Hadid, L. Z. *et al.* Nature of the mhd and kinetic scale turbulence in the magnetosheath of saturn: Cassini observations. *Astrophysical Journal Letters* **813**, (2015).

34. Hadid, L. Z., Sahraoui, F., Galtier, S. & Huang, S. Y. Compressible Magnetohydrodynamic Turbulence in the Earth's Magnetosheath: Estimation of the Energy Cascade Rate Using in situ Spacecraft Data. *Phys Rev Lett* **120**, 1–6 (2018).

35. Grinsted, A., Moore, J. C. & Jevrejeva, S. Application of the cross wavelet transform and wavelet coherence to geophysical time series. *Nonlinear Process Geophys* **11**, 561–566 (2004).

36. Sahraoui, F., Hadid, L. & Huang, S. Magnetohydrodynamic and kinetic scale turbulence in the near-Earth space plasmas: a (short) biased review. *Rev Mod Plasma Phys* **4**, (2020).

37. Santolík, O., Parrot, M. & Lefeuvre, F. Singular value decomposition methods for wave propagation analysis. *Radio Sci* **38**, 1010 (2003).

38. Pincon, J.-L. & Glassmeier, K.-H. Multi-Spacecraft Methods of Wave Field Characterisation. *Unknown* 47–54 (1998).

39. Taylor, G. I. The Spectrum of Turbulence. *Proceedings of the Royal Society A: Mathematical, Physical and Engineering Sciences* **164**, 476–490 (1938).

40. Cho, J. & Vishniac, E. T. The Anisotropy of Magnetohydrodynamic Alfvenic Turbulence. *Astrophys J* **539**, 273–282 (2000).

41. He, J. S. *et al.* Two-dimensional correlation functions for density and magnetic field fluctuations in magnetosheath turbulence measured by the Cluster spacecraft. *J Geophys Res Space Phys* **116**, (2011).

42. Hollweg, J. v. Waves and instabilities in the solar wind. *Reviews of Geophysics* **13**, 263 (1975).

43. Zank, G. P. & Matthaeus, W. H. Waves and turbulence in the solar wind. *J Geophys Res* **97**, 17189 (1992).

44. Saur, J. & Bieber, J. W. Geometry of low-frequency solar wind magnetic turbulence: Evidence for radially aligned Alfvénic fluctuations. *J Geophys Res Space Phys* **104**, 9975–9988 (1999).

Acknowledgments

We would like to thank the members of the *Cluster* spacecraft team, and NASA's Coordinated Data Analysis Web. Data analysis was performed using the IRFU-MATLAB analysis package available at https://github.com/irfu/irfu-matlab and the SPEDAS analysis software available at http://themis.ssl.berkeley.edu.

Author contribution

H. R. Yan initiated and designed the project. S. Q. Zhao and H. R. Yan analyzed the main result of the manuscript. S. Q. Zhao and T. Z. Liu completed the data process methods. All authors contributed to writing, editing, and approving the manuscript

Supplementary information

Details of examination of the turbulence state

To examine the turbulence state, we calclulate the normalized correlation function $R(\tau)/R(0)$, where the correlation function $R(\tau)$ is defined as $\langle \delta B(t) \delta B(t+\tau) \rangle$, τ is the timescale, and the angular brackets represent a time average over the length of the moving time window (5 hours). Figure S1 shows $R(\tau)/R(0)$ for $\delta B_{\perp 1}$ and $\delta B_{\perp 2}$ components of magnetic field fluctuations in field-aligned coordinates. The basis vectors of coordinate axes $\boldsymbol{e}_{\parallel}$, $\boldsymbol{e}_{\perp 1}$, and $\boldsymbol{e}_{\perp 2}$ are in $\widehat{\boldsymbol{b}}_0$, $(\widehat{\boldsymbol{b}}_0 \times \widehat{\boldsymbol{X}}_{GSE}) \times \widehat{\boldsymbol{b}}_0$, and $\widehat{\boldsymbol{b}}_0 \times \widehat{\boldsymbol{X}}_{GSE}$ directions, respectively. $\widehat{\boldsymbol{b}}_0$ is the unit vector of the mean magnetic field in each time window. $\widehat{\boldsymbol{X}}_{GSE}$ is the unit vector towards the Sun from the Earth.

This study estimates the correlation time $T_c \sim \int_0^{R(\tau) \to \frac{1}{2e}} R(\tau)/R(0)\, d\tau$. In Figure S1, $T_c \sim 1400$ s is much less than the time window length (5 hours), suggesting that the fluctuations are approximately stationary. Moreover, the profiles of $R(\tau)/R(0)$ obtained from all time windows are similar and mainly concentrated within one standard deviation (marked by yellow shadows), suggesting that the starting time of the moving time window has a slight influence on $R(\tau)/R(0)$, and thus fluctuations are homogeneous. Above all, it is reasonable to describe structures of turbulent fluctuations using three-dimensional (3D) power distributions.

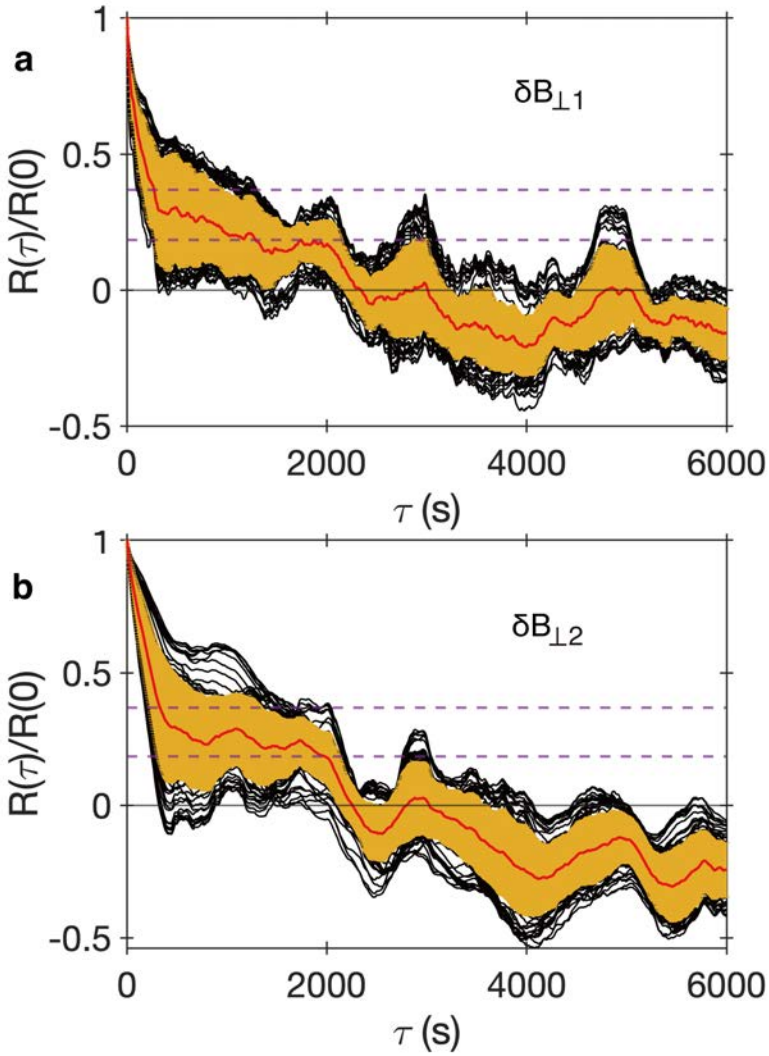

Figure S1: The normalized correlation function $R(\tau)/R(0)$ versus τ for $\delta B_{\perp 1}$ and $\delta B_{\perp 2}$ in field-aligned coordinates. The black curves represent $R(\tau)/R(0)$ from all time windows. The red curves represent average values (s) of $R(\tau)/R(0)$ over all time window. The yellow shaded regions represent $[s-\sigma, s+\sigma]$, where σ represents the standard deviations of $R(\tau)/R(0)$. The purple horizontal dashed lines represent $\frac{R(\tau)}{R(0)} = \frac{1}{e}$ and $\frac{1}{2e}$.

One-dimensional (1D) and two-dimensional (2D) wavenumber distributions of Alfvénic magnetic energy

The 1D wavenumber distributions of Alfvénic magnetic energy are estimated by

$$P_{B_A}(k_\perp) = \sum_{k_\parallel=0}^{k_\parallel \to \infty} \int_0^\infty P_{B_A}(k_\perp, k_\parallel, f_{sc}) df_{sc}\,, \qquad (1)$$

$$P_{B_A}(k_\parallel) = \sum_{k_\perp=0}^{k_\perp\to\infty} \int_0^\infty P_{B_A}(k_\perp, k_\parallel, f_{sc}) df_{sc}. \quad (2)$$

The 2D wavenumber distributions of Alfvénic magnetic energy are estimated by

$$P_{B_A}(k_\perp, k_\parallel) = \int_0^\infty P_{B_A}(k_\perp, k_\parallel, f_{sc}) df_{sc}\,. \quad (3)$$

In Figure S2, 1D wavenumber distributions of Alfvénic magnetic energy from data sets with different angle-θ limits nearly overlap, both for $P_{B_A}(k_\perp)$ and $P_{B_A}(k_\parallel)$. Nevertheless, 1D wavenumber distributions from data sets with θ=10° and 15° show significant deviations from others, which may be responsible for the limited data samples. Due to the limited data samples, we can see many vacant bins are present in 2D wavenumber distributions in Figure S3. With the relaxation of the angle-θ limits, more data samples are involved. Overall, Alfvénic magnetic energy using data sets with different angle-θ limits shows similar wavenumber distributions in Figure S2 and S3.

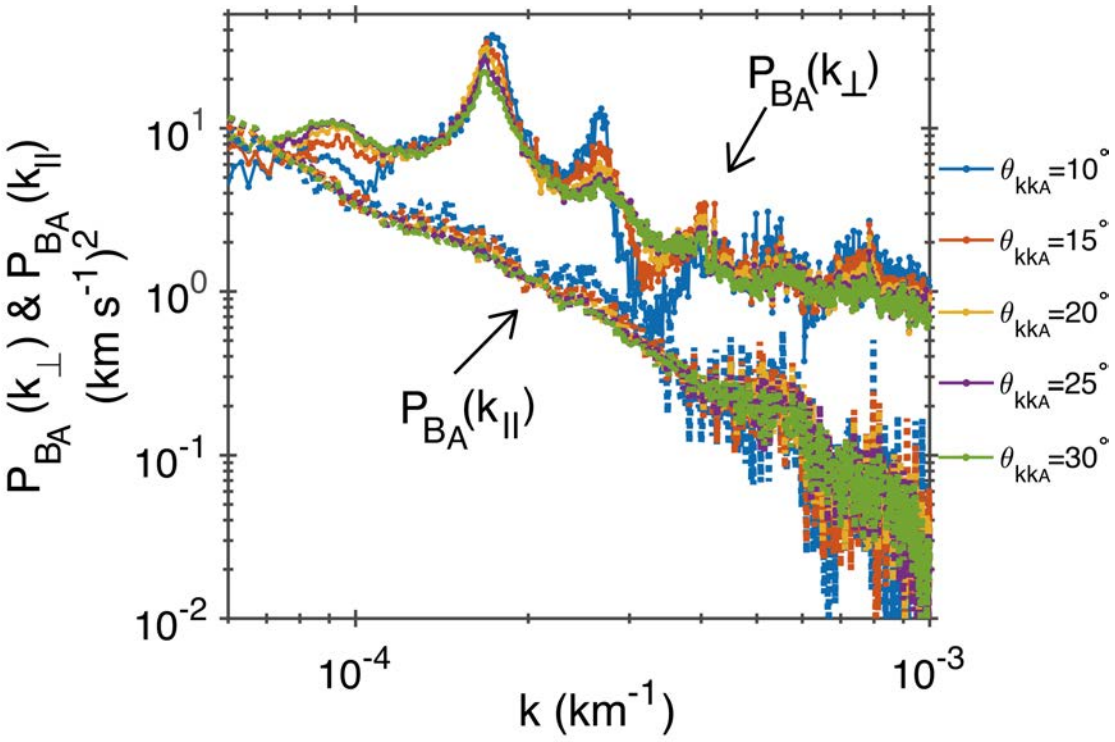

Figure S2: 1D wavenumber distributions of Alfvénic magnetic energy using data sets with θ=10°, 15°, 20°, 25°, and 30°, respectively. $P_{B_A}(k_\perp)$ is displayed by solid curves. $P_{B_A}(k_\parallel)$ is displayed by dotted curves. Blue, red, yellow, purple, and green colors represent observations from data sets with θ=10°, 15°, 20°, 25°, and 30°, respectively.

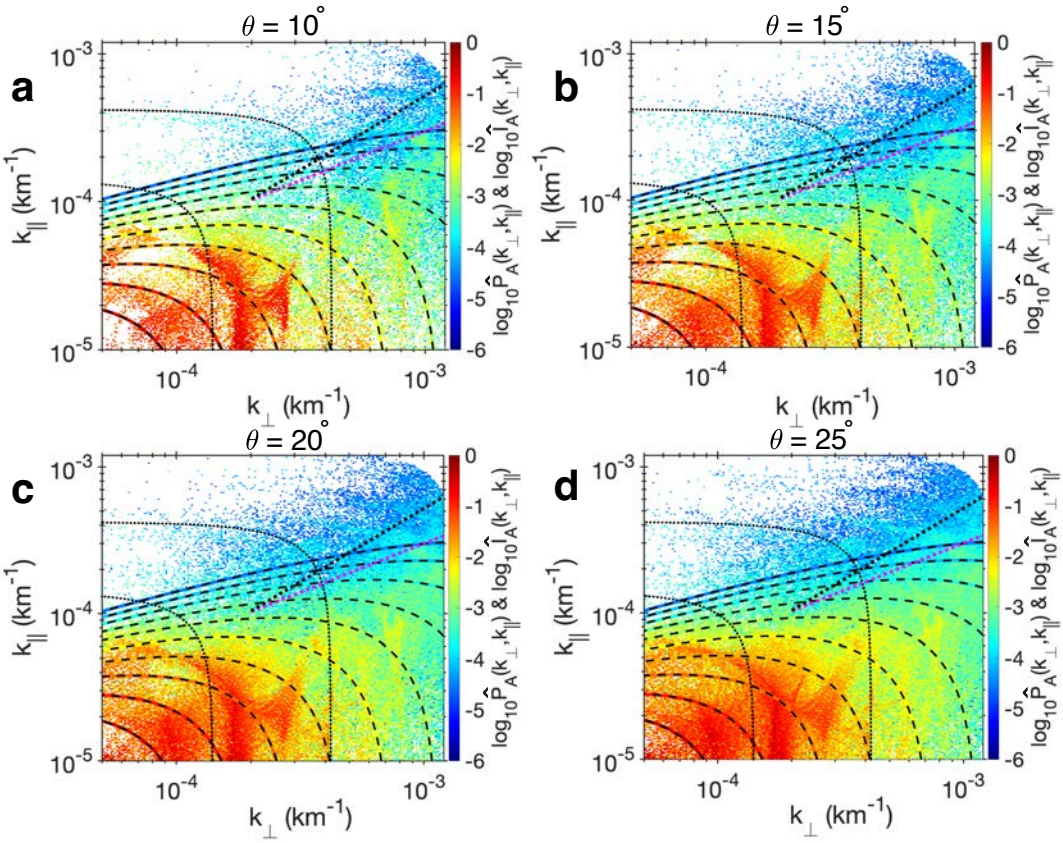

Figure S3: 2D wavenumber distributions of Alfvénic magnetic energy using data sets with θ=10˚, 15˚, 20˚, and 25˚, respectively. For each figure, same format as Fig. 2a. The 2D spectral image represents $\hat{P}_{B_A}(k_\perp, k_\parallel)$. The color contours with black dashed curves represent $\hat{I}_A(k_\perp, k_\parallel)$. $\hat{I}_A(k_\perp, k_\parallel)$ is in the same color map as $\hat{P}_{B_A}(k_\perp, k_\parallel)$. The black dotted curves mark $k = \sqrt{k_\parallel^2 + k_\perp^2} = 0.01/d_i$ and $0.03/d_i$. The pink and black dotted lines represent the scaling $k_\parallel \propto k_\perp^{2/3}$ and $k_\parallel \propto k_\perp$, respectively.

The energy spectra and nonlinear parameters with velocity measurements

We observe a similar Alfvénic weak-to-strong transition with the measurements of velocity fluctuations. The velocity energy spectral density is defined as $E_{V_A}(k_\perp) = \frac{1}{2}\frac{\delta V_A^2(k_\perp)}{k_\perp}$, where the Alfvénic velocity energy density is calculated by $\delta V_A^2(k_\perp) = 2 \times \sum_{k_\perp=k_\perp}^{k_\perp\to\infty} \sum_{k_\parallel=0}^{k_\parallel\to\infty} \int_0^\infty P_{V_A}(k_\perp, k_\parallel, f_{sc}) df_{sc}$. Figure S4a shows the sharp change in spectral slopes of $E_{V_A}(k_\perp)$ from wave-like (-2) to Kolmogorov-like (-5/3). In Figure S4b, for most of the data points, $k_\parallel$ is approximately stable within $k_\parallel \sim [7 \times 10^{-5}, 1 \times 10^{-4}]\ km^{-1}$ in Zone (1), whereas the variation of $k_\perp$ versus $k_\parallel$ agrees with the

scaling $k_{\parallel} \propto k_{\perp}^{2/3}$ in Zone (3). The nonlinearity parameter is estimated as $\chi_{V_A}(k_{\perp}, k_{\parallel}) = \frac{k_{\perp}\delta V_A(k_{\perp},k_{\parallel})}{k_{\parallel}V_A}$, where the Alfvénic velocity energy density is estimated by $\delta V_A^2(k_{\perp}, k_{\parallel}) = \sum_{k_{\perp}=k_{\perp}}^{k_{\perp}\to\infty} \sum_{k_{\parallel}=k_{\parallel}}^{k_{\parallel}\to\infty} \int_0^{\infty} P_{V_A}(k_{\perp}, k_{\parallel}, f_{sc})\, df_{sc}$. Figure S4c shows that, at the corresponding wavenumbers in Figure S4b, χ_{V_A} is much less than unity in Zone (1), whereas χ_{V_A} increases approaching unity and follows the scaling $k_{\parallel} \propto k_{\perp}^{2/3}$ in Zone (3).

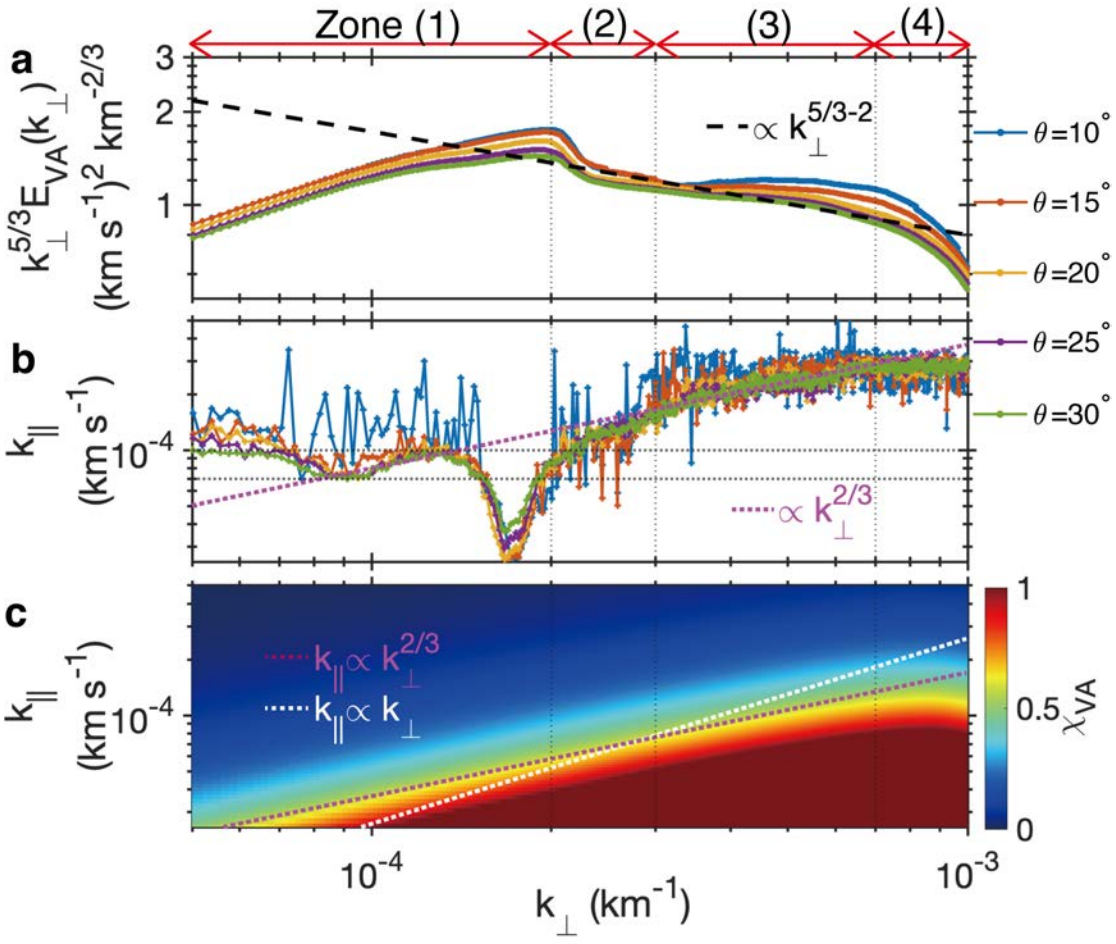

Figure S4: a, The compensated spectra $k_{\perp}^{5/3}E_{V_A}(k_{\perp})$. The black dashed line represents $\propto k_{\perp}^{5/3-2}$. **b**, The variation of $k_{\parallel}$ versus $k_{\perp}$ by taking the same values of velocity energy. The purple dotted line represents the scaling $k_{\parallel} \propto k_{\perp}^{2/3}$. The horizontal dotted lines represent $k_{\parallel} = 7 \times 10^{-5}\, km^{-1}$ and $1 \times 10^{-4}\, km^{-1}$. **a**-**b**, Blue, red, yellow, purple, and green colors represent observations from data sets with θ=10°, 15°, 20°, 25°, and 30°, respectively. **c**, The nonlinearity parameter $\chi_{V_A}(k_{\perp}, k_{\parallel})$. The purple and white

dotted lines represent the scaling $k_{\parallel} \propto k_{\perp}^{2/3}$ and $k_{\parallel} \propto k_{\perp}$, respectively. χ_{V_A} is calculated using the data set with θ=30°. The $k_{\perp}$ distributions are roughly divided into four Zones: Zone (1) $5 \times 10^{-5} < k_{\perp} < 2 \times 10^{-4}\ km^{-1}$, Zone (2) $2 \times 10^{-4} < k_{\perp} < 3 \times 10^{-4}\ km^{-1}$, Zone (3) $3 \times 10^{-4} < k_{\perp} < 7 \times 10^{-4}\ km^{-1}$, and Zone (4) $7 \times 10^{-4} < k_{\perp} < 1 \times 10^{-3}\ km^{-1}$. The first, second, and third vertical dotted lines are around the maximum of $k_{\perp}^{5/3} E_{V_A}(k_{\perp})$, the beginning of flattened $k_{\perp}^{5/3} E_{V_A}(k_{\perp})$, and the end of flattened $k_{\perp}^{5/3} E_{V_A}(k_{\perp})$, respectively.

Schematic of Alfvén mode decomposition from turbulent fluctuations

Figure S5 shows a coordinate in wavenumber space, determined by the unit vectors of the wavevector and background magnetic field ($\hat{\boldsymbol{k}}_{SVD}$ and $\hat{\boldsymbol{b}}_0$). The basis vectors of coordinate axes are in $\hat{\boldsymbol{b}}_0$, $\hat{\boldsymbol{k}}_{\perp,\text{out of } (k_{SVD},b_0) \text{ plane}} = \frac{\hat{\boldsymbol{k}}_{SVD} \times \hat{\boldsymbol{b}}_0}{|\hat{\boldsymbol{k}}_{SVD} \times \hat{\boldsymbol{b}}_0|}$, and $\hat{\boldsymbol{k}}_{\perp,\text{in } (k_{SVD},b_0) \text{ plane}} = \hat{\boldsymbol{b}}_0 \times \hat{\boldsymbol{k}}_{\perp,\text{out of } (k_{SVD},b_0) \text{ plane}}$ directions. The Alfvénic magnetic field and velocity fluctuations are along the $\hat{\boldsymbol{\xi}}_A = \hat{\boldsymbol{k}}_{\perp,\text{out of } (k_{SVD},b_0) \text{ plane}}$ direction. The wavevectors ($\boldsymbol{k}_A$) calculated by multispacecraft timing analysis on Alfvénic magnetic field are not entirely alighted with $\hat{\boldsymbol{k}}_{SVD}$. Thus, we set the angle θ between $\boldsymbol{k}_A$ and $\hat{\boldsymbol{k}}_{SVD}$ as a threshold and only analyze the fluctuations with $\boldsymbol{k}_A$ inside the red cone.

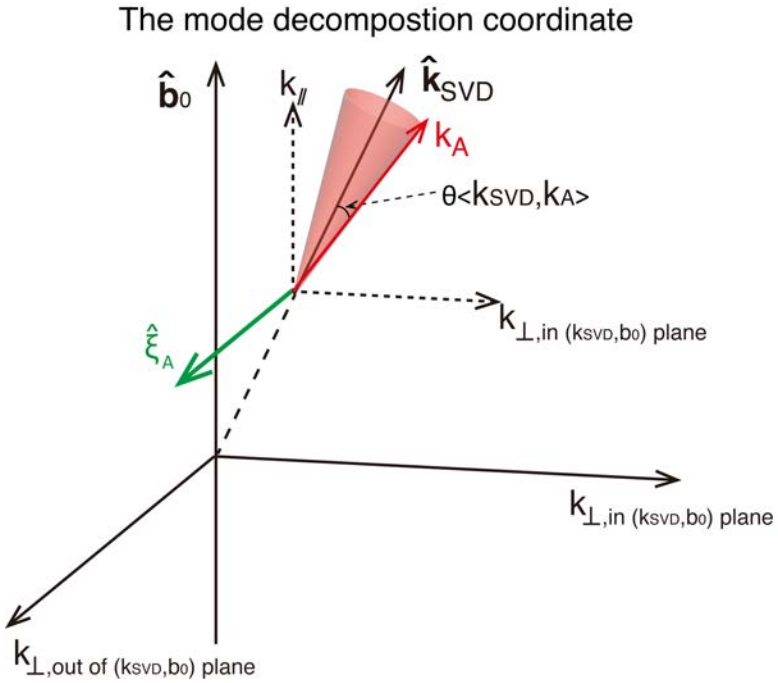

Figure S5: Schematic of Alfvén mode decomposition from the fluctuations.